대한기계학회 2000년도 추계학술대회논문집 B pp. 591~596 KSME 00F212

Finite element analysis of the fluid-structure interaction in a compliant vessel

Eun Bo Shim* • Hyung Jong Ko** • Roger D. Kamm***

유연 혈관에서 유체-고체 상호작용에 대한 유한요소 해석

심 은보, 고 형종, Roger D. Kamm

Key Words : Compliant vessel, fluid structure interaction, flow limitation

Abstract

Flow through compliant tubes with linear taper in wall thickness is numerically simulated by finite element analysis. Two models are examined: a planar two-dimensional channel, and an axisymmetric tube. For verification of the numerical method, flow through a compliant stenotic vessel is simulated and compared to existing experimental data. Computational results for an axisymmetric tube show that as cross-sectional area falls with a reduction in downstream pressure, flow rate increases and reaches a maximum when the speed index (mean velocity divided by wave speed) is near unity at the point of minimum cross-section area, indicative of wave speed flow limitation or "choking" (flow speed equals wave speed) in previous one-dimensional studies. For further reductions in downstream pressure, flow rate decreases. Cross-sectional narrowing is significant but localized. When the ratio of downstream-to-upstream wall thickness is ≤ 2 the area throat is located near the downstream end; as wall taper is increased to ≥ 3 the constriction moves to the upstream end of the tube. In the planar two-dimensional channel, area reduction and flow limitation are also observed when outlet pressure is decreased. In contrast to the axisymmetric case, however, the elastic wall in the two-dimensional channel forms a smooth concave surface with the area throat located near the mid-point of the elastic wall. Though flow rate reaches a maximum and then falls, the flow does not appear to be choked.

1. Introduction

In many practical situations the fluid dynamic forces acting on a physiologic vessel cause the walls to undergo significant deformation. These deformations frequently influence the rate of flow through the vessel and can also elicit important biological effects. Examples in the first category include collapse of the veins above the level of the heart, flow limitation during a forced expiration, and the "waterfall effect" in the pulmonary microvascular bed[1]. Other, biological effects arise from the deformation of the vessel wall, resulting in altered gene expression or secretion of various agents, cytokines or growth factors, for example.

Numerous studies have been conducted on vessel collapse using experimental or numerical methods. Experiments by Conrad[2] and Bertram[3], to name a few, have demonstrated the rich variety and complexity associated with such phenomena as flow limitation and self-excited oscillations. Questions still remained, however, concerning the precise physical mechanism of flow instability in certain types of flutter and, because of the simplifying assumptions on which the analyses were based, they were obviously not capable of addressing issues involving two- or three-dimensional effects.

In order to produce a more realistic simulation, Pedley[4] first examined steady, two-dimensional flow in a collapsible channel at low Reynolds number using lubrication theory. Extending this work, Luo & Pedley[5] solved the full Naiver-Stokes equations for steady and unsteady flow, again for a two-dimensional collapsible channel. In these studies, the wall was modeled as an elastic membrane having zero thickness. This is a useful simplification for thin-walled vessels but one which fails to account for bending stiffness and in-wall shear stresses that are important in a wall of finite thickness,

* 금오공대 기계공학부 조교수
** 금오공대 기계공학부 부교수
*** MIT, 기계공학과 및 의공학 전공 교수

and which provides no information on the stress distribution inside the vessel wall. More recently, Heil [6] produced a three-dimensional solution of flow through a collapsible tube using a Stokes flow approximation for the fluid and a shell model for the wall. His results accurately reproduce the three-dimensional character of vessel collapse and compare favorably with experiments but have thus far been restricted to low Reynolds number flow and thin-walled vessels.

Using a finite element code that solves the fully nonlinear equations for the solid and fluid, Bathe & Kamm[7] recently analyzed flow at high Reynolds number through an axisymmetric stenotic vessel. Though the axisymmetric assumption precluded buckling of the wall, the solutions allowed for significant inertial effects in the fluid and provided detailed information on the stress field within the elastic wall. The deformations computed in that work, however, were relatively small due to the stiffness of the arterial wall and stenosis relative to the magnitude of pressure fluctuations.

In this study we use the same approach as Bathe & Kamm[7], but consider two problems with large amplitude wall deformations. In an attempt to minimize the influence of the downstream rigid attachment point, models of tubes and channels are used that have a linear taper in wall thickness. Flow is induced by a progressive reduction in downstream pressure. Steady solutions for given pressure differences are obtained solving the full Navier-Stokes equations and the equilibrium equations for the solid elastic wall having finite thickness. We examine varying degrees of wall taper to elucidate its effect on vessel collapse. A commercial finite element package ADINA is employed to accurately simulate the essential character of fluid-structure interactions. To validate the accuracy of the code, we solve for flow and deformation in a stenotic compliant tube and two-dimensional collapsible channel, and compare the numerical predictions to existing experimental and numerical data.

2. Computational Model and Methods

Two geometries are simulated to investigate flow through flexible-walled vessels, using the commercial package ADINA (Automatic Dynamics Incremental Nonlinear Analysis, Watertown, MA). Response of the elastic wall is analyzed using the standard Lagrangian formulation for which the governing field equations evaluated at each time step in the analysis are

$$\tau_{ij,i}=\rho_s \ddot{u}_i \qquad (1)$$

where τ_{ij} is the ijth component of the Cauchy stress tensor (i,j = 1,2), $\ddot{u}_i$ is the material particle acceleration in the coordinate i direction, and ρ_s is the density of solid. The comma denotes partial differentiation. ADINA uses a mixed displacement/pressure-based finite element formulation to solve these equations. In the solutions presented here, nine-node axisymmetric quadrilateral elements with quadratic displacement interpolation and linear element pressure are employed.

The governing equations for viscous incompressible fluid flow are obtained from the principles of mass and momentum conservation. The equations in vector notation are

$$\frac{\partial U}{\partial t}+\nabla\cdot(F-G)=0 \qquad (2)$$

where

$$U=\begin{bmatrix}0\\ \rho_f\vec{v}\end{bmatrix},\quad F=\begin{bmatrix}\rho_f\vec{v}\\ \rho_f\vec{v}\vec{v}\end{bmatrix},\quad G=\begin{bmatrix}0\\ \tau\end{bmatrix} \qquad (3)$$

and where $\vec{v}$ is the velocity vector; ρ_f is fluid density, and τ is the stress tensor, the components of which are given by:

$$\tau_{ij}=-p\delta_{ij}+2\mu e_{ij} \qquad (4)$$

Here p is fluid pressure, δ_{ij} the Kronecker delta, μ the coefficient of viscosity, and the components of the strain rate tensor are given by

$$e_{ij}=\frac{v_{i,j}+v_{j,i}}{2} \qquad (5)$$

Application of the usual Galerkin finite element discretization for equation (2) yields the following matrix equations in symbolic form:

$$\mathbf{KX = R} \qquad (6)$$

where **K** is the stiffness matrix, **X** is the vector of unknown nodal variables (velocities and pressure) and **R** contains the external driving forces. Three-node axisymmetric triangular elements with a linear interpolation function for velocity and pressure and an additional bubble velocity function are used to discretize the fluid domain in equation (2). Since the matrix equation above, derived from fluid governing equation (2), is highly nonlinear it must be solved by an incremental iterative scheme such as the Newton-Raphson method or the method of successive substitution within each time step[8]. A similar matrix equation for the solid is derived from application of the variational principle to equation (1) and discretization of the solid solution domain with nine-node axisymmetric quadrilateral elements having a quadratic displacement interpolation function. In the solid matrix equation, the unknown variables are the nodal displacement vectors.

To simulate interactions between the fluid and solid domains, ADINA utilizes the Arbitrary Lagrangian Eulerian (ALE) formulation [8] requiring that the momentum equation in (2) be modified to account for mesh movement.

3. Results and Discussion

3.1 Verification of the code

In order to test the FSI capabilities of the code, we solve for steady flow through a stenotic compliant tube and compare our results with existing experimental data [9]. For this computation the working fluid is water and the membrane is made of rubber, modeled here using the Mooney-Rivlin description. The ratio of bulk modulus to shear modulus is set equal to 1500, giving a Poisson ratio of 0.4997 in this linear elastic analysis. The geometry of the stenotic tube is shown in Fig. 1(a), selected to mimic that used in the Stergiopulos experiments. As seen in the figure, the stenosis extends for a length of L_s=30 mm and has an unobstructed diameter D_0 of 8 mm. The stenosis diameter at zero transmural pressure D_s is 2.53 mm so that the severity of the stenosis defined as $\left[1-D_s^2/D_s^2\right]\times 100 = 90\%$. We use the following equation for the shape of the stenosis as is in the case of Stergiopulos's experiment[9].

$$D(x) = D_0 - \frac{D_0 - D_s}{2}\left[1-\cos\left(\frac{2\pi x}{L_s}+\pi\right)\right] \qquad (7)$$

The mesh system of the fluid region is composed of 4,848 triangular elements and 2,639 nodes and 122 elements and 315 nodes in solid domain.

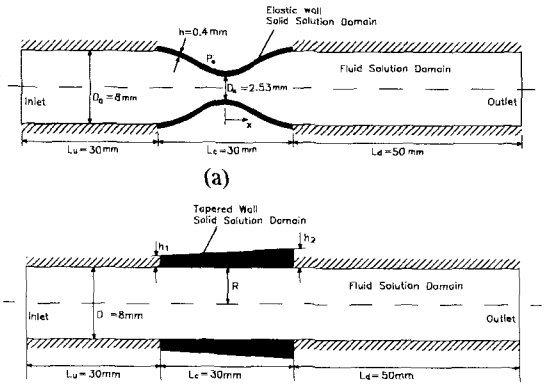

Figure 1. Tube and channel geometries from the present simulations: (a) The stenotic tube with elastic wall as used in the study by Stergiopulos et al.[9]. (b) Axisymmetric compliant tube.

During the simulation, inlet pressure is held constant at a value of P_{in} = 74 mmHg and outlet pressure P_{out} is decreased from 74 mmHg in 1 mmHg increments. External pressure P_e is maintained constant at 3 mmHg. At each pressure, the simulation is continued until the solution becomes steady. This procedure is followed until P_{out} = 41 mmHg, at which point the numerical solution is no longer able to converge. Since at this stage the Reynolds number based on average outlet velocity and unobstructed diameter is 2478, solutions for lower downstream pressures would be strongly influenced by turbulence, the effects of which are absent from our analysis. In addition, as discussed below, the transmural pressure is beyond that needed to buckle the tube, thus invalidating the assumption of axisymmetry. Thus, while the cause of the solution breakdown is unknown, there is good reason based on physical grounds, not to attempt to continue the solution any further since the results would be increasingly unrealistic.

The streamlines obtained from this solution exhibit a large region of recirculating flow downstream of the stenosis, as one would expect in the vicinity of a sudden expansion. Pressure attains a minimum value at the throat, raising the possibility of collapse of the stenotic tube at that point. Progressing downstream from the stenosis, the pressure increases, corresponding to flow deceleration with some pressure recovery. Figs. 2(a) & (b) show the variations of flow rate and internal diameter of the stenosis as functions of outlet pressure. When the pressure difference is small, there is good agreement between the measured and predicted flow rates and internal diameter of the stenosis. As the pressure difference increases, however, the numerical solutions deviate some from the experimental values, and the computations are terminated at a pressure difference of 41 mmHg prior to the point where the experimental results show flow limitation and tube collapse.

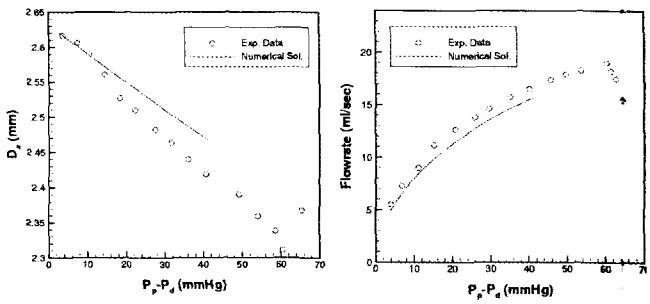

Figure 2. Comparisons of computed results to experimental data by Stergiopulos, et al.[9]; (a) Stenotic diameter versus pressure difference. (b) Flow rate versus pressure difference.

3.2 Axisymmetric tube with tapered wall

The axisymmetric model used in the first set of simulations is shown in Fig. 1(b). Here, h_1, the upstream wall thickness, is held constant at 0.4 mm. Wall thickness tapers linearly to a minimum value, h_2, at the downstream end. The tube length-to-radius ratio, L_c/R, is equal to 7.5 and tapers h_2/h_1 of 1, 2, 3, and 4 are used. The tube wall is taken to be linearly elastic with Young's

modulus of 2 x 10^3 Pa. All other parameter values are given in Table 1.

Table 1. Material properties and reference values used in simulations of an axisymmetric compliant tube.

Fluid density : ρ	10^3 kg/m^3
Fluid viscosity : μ	10^{-3} kg/(m·s)
Elastic modulus of solid : E	2 x 10^3 N/ m^2
Poisson ratio of solid : ν	0.3
Unobstructed area : $A_0=\pi R^2$	5 x 10^{-4} m^2
Reference pressure : $P_{ref}=Eh_1/R$	200 Pa
Flow rate $Q_{ref}=\pi R^2\cdot(Eh_1/\rho D_0)^{1/2}$	15.8 ml/s

A no slip wall boundary condition is applied in the fluid along lines AB and CD while symmetry is assumed around line EF. Line BC coincides with line IJ of the solid domain constituting the fluid-structure interaction boundary (Fig. 3). It is along this boundary that displacements and traction forces are passed between the fluid and solid domains. In these simulations, the fluid and solid domains are discretized as shown in Fig. 4. The mesh consists of 3,383 nodes, 6,227 triangular elements clustered in both ends of the elastic wall for the fluid domain and 140 quadrilateral elements for the solid domain. To assess mesh dependency, computational results using finer (one third more mesh points) and coarser (one third fewer) mesh points for h_2/h_1 = 1 produced differences in flow rate and minimum area reduction of less than 2.5 %.

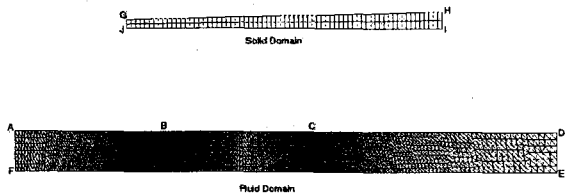

Figure 3. Mesh system for the axisymmetric tube with 6,227 triangular fluid elements and 140 quadrilateral solid elements.

Flow is induced by the pressure difference $\Delta P = P_{in} - P_{out}$ between inlet and outlet. Inlet pressure and external pressure are maintained constant at $P_{in} = P_e = 0$ while downstream pressure is decreased in 5 Pa increments, allowing the solution to converge at each condition. The computations are conducted in a step-wise manner using the steady solution from the previous step as the initial guess for the next calculation.

Figure 4 shows flow rate increasing as downstream pressure is reduced, rapidly at first, then slowing, reaching a maximum, and finally falling gradually as the tube becomes increasingly collapsed. This pattern is suggestive of wave speed flow limitation as is often observed in collapsible tube flow, although the drop in flow rate after reaching the peak is not predicted by the previous one-dimensional theories. This behavior is discussed more fully below.

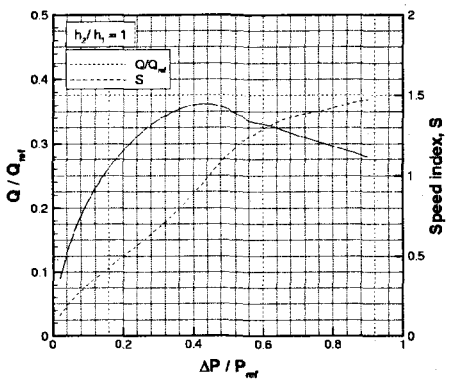

(a)

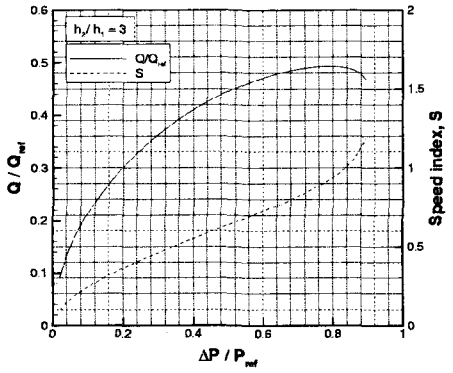

(b)

Figure 4. Flow rate and speed index as functions of the inlet-to-outlet pressure difference for (a) h_2/h_1 = 1, (b) h_2/h_1 = 3.

When the degree of wall taper is large (h_2/h_1 = 3 or 4), the behavior is distinctly different. The point of minimum area moves to a location near the upstream end of the tube, and the recirculation zone is less pronounced or completely absent due to the more gradual area increase downstream. Variations in minimum area are particularly interesting showing, in contrast to cases with milder taper, an increasingly steep drop as downstream pressure is reduced, up to the point of non-convergence (Fig. 5). Flow limitation, however, is observed (Fig. 4) and follows a pattern that is relatively uninfluenced by the degree of taper. These solutions tend to lose convergence soon after maximal flow is attained.

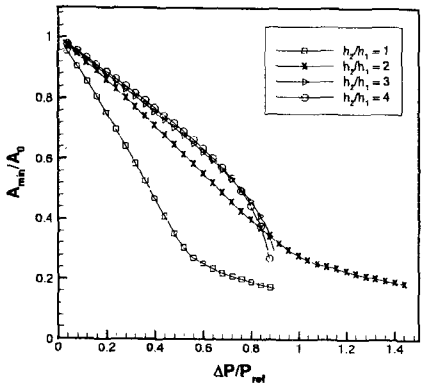

Figure 5. Minimum cross-sectional area in the axisymmetric tube as a function of the inlet-to-outlet pressure difference. Note the difference in character at high collapse for the two cases with large taper as compared to those with small taper.

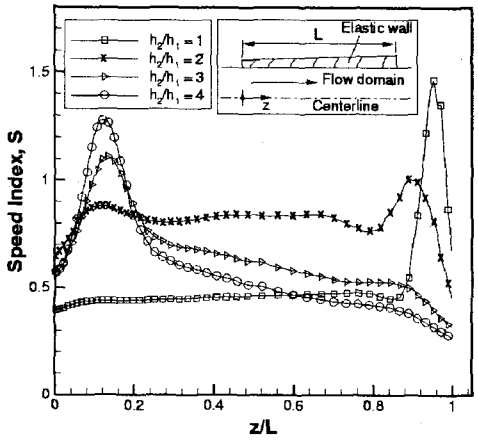

Figure 6. Distribution of speed index as a function of axial distance along the axisymmetric tube at $\Delta P/P_{ref}$ = 0.6 for each of the four tapered wall configurations.

In view of the tendency for flow limitation seen in these results, it is of interest to compute the speed index, S, defined as the ratio of mean fluid speed to wave speed. Here we estimate wave speed for long waves, c, using the Moens-Korteweg equation[10].

$$c = (Eh/2\rho_f R)^{1/2} \qquad (8)$$

In a one-dimensional flow analysis, maximal flow occurs when S equals unity[3]. This is seen to be true in the present simulations (Figure 6) when the speed index evaluated at the point of minimum cross-sectional area, based on centerline velocity, is plotted against the pressure difference. Unlike the prediction from purely one-dimensional theory, however, the flow rate is observed to decrease and S continues to rise as downstream pressure is further reduced. Moreover, the profile of S vs. axial distance, z/L (Fig. 6) continues to change upstream of the point where S=1, albeit slightly, following the first occurrence of critical flow. These observations could be due to the presence of longitudinal bending stiffness or tension, either of which introduce wave speed dispersion (so that waves of finite wavelength travel more rapidly than predicted by eqn. (9))[11]. In fact, the possibility of a transition to supercritical flow (S>1) near the downstream attachment point had been observed experimentally and tentatively explained based on an approximate correction to the one-dimensional theory that includes these longitudinal effects (Kececioglu et al., 1981).

With larger taper (h_2/h_1 = 3 and 4, Fig 4(b)), the flow rate once again reaches a maximum when S is approximately one. The fall in flow rate and the increase in speed index after the point of maximal flow, however, are both more abrupt, and the solution fails to converge much sooner.

Note that in these cases, the point of minimum area and the first occurrence of critical flow are both located near the upstream end of the tube. Downstream of this point the flow accelerates beyond S=1, then quickly decelerates to subcritical speeds, continuing to fall in the direction of increasing stiffness. While the transition to subcritical speed appears to be smooth as suggested in previous experiments and one-dimensional theory for tubes with tapered[11], the axisymmetric assumption of the present analysis makes it difficult to make a direct comparison.

3.3 Two-dimensional channel with tapered wall

Of the many theoretical or numerical studies on a collapsible channel, most have invoked the assumption that the wall can be modeled as a thin membrane instead of solving the governing equations for solid. Consequently, they cannot be used to examine a collapsible channel with tapered wall.

A planar geometry similar to that of the axisymmetric tube is adopted (Fig. 1(b)), but with the diameter replaced by the channel height H. On the assumption of symmetry, the computational domain is taken to be the upper half of the channel. Reference quantities and material properties are given in Table 2.

Table 2. Material properties and reference values in two-dimensional collapsible channel.

Fluid density : ρ	10^3 kg/m^3
Fluid viscosity : μ	10^{-3} kg/(m·s)
Elastic modulus of solid : E	2×10^5 N/ m^2
Poisson ratio of solid : ν	0.3
Pressure : $P_{ref} = E[h_1/(H/2)]^4$	0.2 Pa
Flow rate : $Q_{ref} = H \cdot (P_{ref}/\rho)^{1/2}$	1.14×10^{-4} m^2/s

As in the axisymmetric tube, flow is induced by decreasing the outlet pressure while inlet pressure is held constant at zero. Wall tension is zero in the undeformed state. Flow rate, plotted as a function of pressure drop in Fig. 7, rises to a maximum as downstream pressure is reduced, then, in contrast to the axisymmetric tube, falls and asymptotically approaches zero. Maximal flow rate increases with increasing wall taper, reflecting the increase in average wall thickness and the consequent delay in wall deflection.

Unlike the axisymmetric tube, wave speed in a two-dimensional channel is entirely determined by axial bending stiffness and tension, and approaches zero in the limit of long waves. Therefore the speed index is ill-defined as are the concepts of choking or wave speed flow limitation. Consistent with this, there appears to be no qualitative change in flow behavior after the peak in flow rate; height and mean flow speed continue to decrease along the entire length of the channel as downstream pressure is further reduced.

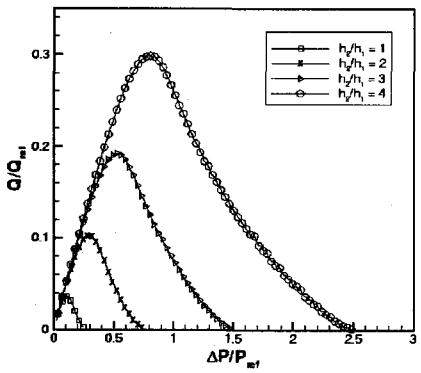

Figure 7. Flow rate in the two-dimensional channel as a function of inlet-to-outlet pressure difference.

4. Conclusion

In this paper, we used the full Navier-Stokes equations to describe flow within the collapsible tube, and allowed for a wall with finite thickness that undergoes large deformation. These are all necessary if a realistic simulation is to be created. The true flow field occurring in collapsible tube interacting with an elastic wall has complicated characteristics certain to be influenced by viscous dissipation and possibly flow separation behind the throat of elastic wall. These effects cannot be simulated with inviscid or Stokes flow assumptions. Furthermore, while most previous studies approximate the collapsible tube or channel as a membrane of zero-thickness, many of the existing experiments and real occurrences of collapsible tube flow in physiology deal with tubes that are not necessarily thin.

Numerical solutions for the collapsible tube show that flow rate reaches a maximum when the speed index is near unity at the point of minimum cross-sectional area, indicative of flow limitation or choking. The constriction points in the tube vary according to the ratio of downstream-to-upstream wall thickness.

References

(1) R. D. Kamm and T. J. Pedley, "Flow in Collapsible Tubes: A brief Review", ASME Tran. J. of Biomechanical Engineering, Vol. 111, pp. 177-179, 1989.

(2) W. A. Conrad, "Pressure-Flow Relationalships in Collapsible Tubes", IEEE Trans. Biomedi. Engng., Vol. 16, pp. 284-295, 1969.

(3) C. D. Bertram, 1986, Unstable Equilibrium Behavior in Collapsible Tubes, J. of Biomechanics, Vol. 19, pp. 61-69, 1986.

(4) T. J. Pedley, "Longitudinal Tension Variation in a Collapsible Channel: a New Mechanism for the Breakdown of Steady Flow", ASME Trans. J. Biomech. Eng., Vol 99, pp. 126-147, 1992.

(5) X. Y. Luo and T. J. Pedley, "A Numerical Simulation of Steady Flow in a 2-D Collapsible Channel", J. Fluids and Struct., Vol. 9, pp. 149-174, 1995.

(6) M. Heil, "Stokes Flow in a Collapsible Tubes: Computation and Experiment", J. Fluid Mechanics, Vol. 353, pp. 285-312, 1997.

(7) M. Bathe and Kamm, R.D., 1998, A Fluid-Structure Interaction Finite Element Analysis of Pulsatile Blood Flow through a Compliant Stenotic Artery, *ASME Tran. J. of Biomechanical Engineering*, ASME J. Biomech. Eng., Vol. 121, pp. 361-369, 1999.

(8) K. J. Bathe, H. Zhang and M. H. Wang, "Finite Element Analysis of Incompressible and Compressible Fluid Flows with Free Surfaces and Structural Interactions", Computers and Structures, Vol. 56, pp. 193-213, 1995.

(9) N. Stergiopulos, J. E. Moore, A. Strassle, D. N. Ku and J. J. Meister, "Steady Flow Tests and Demonstration of Collapse on Models of Compliant Axisymmetric Stenosis", Adavanced in Bioengineering BED, Vol. 26, pp. 455-458, 1993.

(10) C. G. Caro, T. J. Pedley, R. C. Schroter and W. A. Seed, The Mechanics of the Circulation, Oxford, Oxford University Press, 1978.

(11) M. E. McClurken, I. Kececioglu, R. D. Kamm, A. H. Shapiro, "Steady Supercritical Flow in Collapsible Tubes : Part 2. Theoretical Studies", J. Fluid Mech., Vol. 114, pp. 60-67, 1981.